Chapter 3

SYNTHETIC OBSERVATIONAL DIAGNOSTICS

Just remember this, my girl,
When you look up in the sky
You can see the stars
And still not see the light,
That's right.

Jack Tempchin & Robb Strandlund, *Already Gone*

In order to compare theoretical models with observations, one must be able to compute the emergent photon distribution from these models and transform such noise-free "data" into a form where a one-to-one comparison with actual data is possible. The presence of hot-star winds has been inferred from radio, infrared, visible, ultraviolet and X-ray observations, but here we concentrate mainly on ultraviolet wavelengths, which are the most luminous for early-type stars. The major goal of this Chapter is to compute the shapes and strengths of P Cygni type spectral lines from an expanding envelope around a star (Section 3.1). Also, in anticipation of subsequent Chapters dealing with highly structured and inhomogeneous winds, a simple form of the continuum polarization from non-spherical and optically thin circumstellar gas distributions is derived (Section 3.2).

3.1 P Cygni Spectral Line Formation

3.1.1 The Source Function of the Radiation Field

Although the source function S_ν was not seen to have a crucial impact on the derivation of the radiation force in Section 2.2, it will be very important when calculating the shapes and strengths of spectral lines formed in the stellar wind.

Let us then evaluate the source function using the "escape probability" formalism of Sobolev (1957) and Castor (1970).

Consider the formal solution to the equation of radiative transfer, given by eq. (2.25),

$$I_\nu(\tau_\nu) = \int_0^{\tau_\nu} S_\nu(t_\nu) e^{-(\tau_\nu - t_\nu)} dt_\nu \; + \; I_\nu^{\rm core} e^{-\tau_\nu} \quad . \tag{3.1}$$

The optical depth is given in the Sobolev approximation by

$$\tau_\nu(\mathbf{r}) = \tau_o(\mathbf{r})\, \Phi(x, \mathbf{r}) \quad , \tag{3.2}$$

where the Sobolev optical depth τ_o and the integrating factor $\Phi(x, \mathbf{r})$ are defined and discussed above in Section 2.2. Note, however, that the same approximations which allowed τ_o to be taken outside the depth integral also allow the source function S_ν to be considered roughly *constant* over a Sobolev length $L_{\rm Sob}$. Thus,

$$I_\nu(\tau_\nu) = S_\nu(\tau_\nu) \left[1 - e^{-\tau_\nu}\right] \; + \; I_\nu^{\rm core} e^{-\tau_\nu} \quad . \tag{3.3}$$

Although the frequency dependence of the intensity and emergent flux will eventually be required to compute line profiles, it is the *frequency averaged* intensity which is needed for the source function to be found. The thermal Doppler motions in the gas, which are dominant in the Sobolev approach, tend to produce complete frequency distribution in the inertial frame. The source function that appears in the radiative transfer will thus be a quantity that is averaged over the line's frequency domain:

$$\bar{S}(\mathbf{r}) \equiv \int_{-\infty}^{+\infty} \phi(x)\, S_\nu(\mathbf{r})\, dx \tag{3.4}$$

(here x is the dimensionless Doppler frequency defined in eq. [2.20]), and the formal solution for the intensity can be similarly averaged over the line,

$$\bar{I} = \bar{S} \left[1 - \left(\frac{1 - e^{-\tau_o}}{\tau_o}\right)\right] + \bar{I}^{\rm core} \left(\frac{1 - e^{-\tau_o}}{\tau_o}\right) \quad , \tag{3.5}$$

using the analytic integral evaluated in eq. (2.38). The quantity in parentheses

$$p(\hat{\mathbf{n}}) = \frac{1 - e^{-\tau_o}}{\tau_o} \tag{3.6}$$

can be considered the probability (dependent on the angle $\hat{\mathbf{n}}$ in the Sobolev optical depth) of escape from the circumstellar region by a locally-scattered line photon.

In addition to the average over line frequency, consider an average (i.e., zeroth moment) of the formal intensity solution over solid angle:

$$4\pi \bar{J} = \oint \bar{I} d\Omega = \bar{S} \left[4\pi - \oint p(\hat{\mathbf{n}})\, d\Omega\right] + \oint \bar{I}^{\rm core}(\hat{\mathbf{n}})\, p(\hat{\mathbf{n}})\, d\Omega \quad . \tag{3.7}$$

This expression allows one to solve explicitly for the angle and frequency independent source function. If isotropic scattering and LTE are assumed, then

$$\bar{S} = \bar{\epsilon}\, B_\nu(T) + (1-\bar{\epsilon})\, \bar{J} \ , \tag{3.8}$$

where $\bar{\epsilon}$ is a line-averaged photon destruction probability per scattering, and the Planck function $B_\nu(T)$ is considered slowly-varying over the line. Note that the probability $\bar{\epsilon}$ (which ranges between 0 and 1) is sometimes replaced by $\bar{\epsilon}'$, the ratio of collisional to radiative deexcitation, where $\bar{\epsilon}' = \bar{\epsilon}/(1-\bar{\epsilon})$ ranges between 0 and $+\infty$, and is proportional to the gas density:

$$\bar{\epsilon}' \ = \ \epsilon_o' \left(\frac{\rho}{\rho_o} \right) \ \ ; \qquad \bar{\epsilon} \ = \ \frac{\epsilon_o(\rho/\rho_o)}{(1-\epsilon_o) + \epsilon_o(\rho/\rho_o)} \ , \tag{3.9}$$

where $\epsilon_o = \epsilon_o'/(1+\epsilon_o')$ is a convenient density-independent probability. Solving the above equation for $\bar{J}$, then, gives the source function in terms of intensity moments and escape probabilities:

$$\bar{S}(\mathbf{r}) = \frac{4\pi\bar{\epsilon}\, B_\nu(T) + (1-\bar{\epsilon}) \oint \bar{I}^{\rm core}(\hat{\mathbf{n}})\, p(\hat{\mathbf{n}})\, d\Omega}{4\pi\bar{\epsilon} + (1-\bar{\epsilon}) \oint p(\hat{\mathbf{n}})\, d\Omega} \ . \tag{3.10}$$

This general expression is often simplified in practice. Most spectral lines observed in winds are pure-scattering resonance lines, so $\bar{\epsilon} \approx 0$. Also, the stellar "core" intensity can be expressed as the product of a constant continuum-like term and a limb-darkening function,

$$\bar{I}^{\rm core}(\hat{\mathbf{n}}) \ \equiv \ I^C D(\hat{\mathbf{n}}) \ , \tag{3.11}$$

and under these two approximations,

$$\bar{S} \ \approx \ \frac{I^C \oint D(\hat{\mathbf{n}})\, p(\hat{\mathbf{n}})\, d\Omega}{\oint p(\hat{\mathbf{n}})\, d\Omega} \ \equiv \ \frac{I^C \beta_c}{\beta} \ , \tag{3.12}$$

where the angle-averaged escape probability is denoted by β, and the probability of a photon escaping the local region and then intercepting the core (the "core penetration probability") is denoted by β_c. If one assumes a perfectly isotropic photon distribution, one can approximate $\beta_c \approx \beta W$, where W is the standard dilution factor (probability of a random ray $\hat{\mathbf{n}}$ intercepting the core).

This escape probability formalism for $\bar{S}$ is a valuable tool, but it has its limits. Recall that the Sobolev approximation requires the velocity to be monotonically varying along all rays pointing away from the star. This, however, is not guaranteed in the multidimensional and time-dependent wind models presented in subsequent Chapters. Winds with nonmonotonic velocity fields have *nonlocal* line forces, since

multiple resonance surfaces can create additional attenuation of the stellar flux (Rybicki & Hummer 1978; Puls, Owocki, & Fullerton 1993, hereafter POF). Multiple resonances can also occur in the presence of line multiplets, but the Sobolev escape probability formalism can be easily modified in this case (see, e.g., Olson 1982). POF compare the use of the local Sobolev method with a self-consistent multiple-resonance technique in structured wind models, and find significant disagreement in the resulting line profiles. However, our hydrodynamical models of large-scale inhomogeneities in winds are much less structured than the one-dimensional instability (small-scale shock) models used by POF, with far fewer zones of nonmonotonic velocity variation in the entire wind. We thus use the escape probability approximation for $\bar{S}$ in all theoretical line profiles in this work, and model the presence of small-scale shocks by *microturbulence* (see Section 3.1.3, below).

3.1.2 The Emergent Intensity and Flux

The radiative flux from a spherical star is a purely radial vector with magnitude

$$\mathcal{F}_\nu \;=\; \int_{\phi'=0}^{2\pi} \int_{\mu'=\mu_*}^{1} I_\nu(\mu',\phi')\,\mu'\,d\mu'\,d\phi' \quad , \tag{3.13}$$

where the angles $\theta' = \cos^{-1}\mu'$ and ϕ' are measured from a position in the wind a distance r from the origin, and

$$\mu_* \;=\; \sqrt{1-\frac{R_*}{r}} \tag{3.14}$$

defines the stellar limb from this position. The local cylindrical coordinate system (p',ϕ',z') is useful to define, with

$$p' \;=\; r\sin\theta' \;=\; r\sqrt{1-\mu'^2} \tag{3.15}$$

$$z' \;=\; r\cos\theta' \;=\; r\mu' \quad , \tag{3.16}$$

and the flux integral, for an observer along the positive z'-axis at an infinite distance from the origin ($r \to \infty$), can be rewritten as

$$\mathcal{F}_\nu \;=\; \frac{1}{r^2}\int_{\phi'=0}^{2\pi} \int_{p'=0}^{R_*} I_\nu(p',\phi',z'\to\infty)\,p'\,dp'\,d\phi' \quad . \tag{3.17}$$

Line profiles are frequently written in terms of a residual flux $\mathcal{R}_\nu \equiv \mathcal{F}_\nu^L/\mathcal{F}_\nu^C$, where the line flux $\mathcal{F}_\nu^L$ uses the full formal solution for I_ν, and the continuum flux $\mathcal{F}_\nu^C$ uses the unattenuated stellar intensity $I_\nu^{\rm core}$.

The flux from a spectral line formed primarily in the *wind,* however, involves more than just an integration over the stellar surface. Formally, the integral over

p' must range from zero to infinity, but in practice we set a maximum radius $R_{\max}$ in all models, beyond which the density and emissivity are negligibly small. Castor (1970), Rybicki & Hummer (1978), and Castor & Lamers (1979) computed P Cygni type line profiles using the Sobolev approximation and a parameterized wind model to compute the intensity and optical depth. The Sobolev intensity in the line is given by eq. (3.3), and for an intrinsic line profile which is much thinner than the expected wind-broadened profile (i.e., for $v_{th} \ll v_\infty$), the integrated profile function is a step function which jumps at the *resonance point,*

$$\Phi(x, \mathbf{r}) \;=\; \begin{cases} 0, & x < \hat{\mathbf{n}} \cdot \mathbf{v}/v_{th} \\ 1, & x \geq \hat{\mathbf{n}} \cdot \mathbf{v}/v_{th} \;\; , \end{cases} \tag{3.18}$$

where here $\hat{\mathbf{n}} = \hat{\mathbf{e}}_{z'}$ because the observer is along the $+z'$ axis.

Note that, since the stellar disk occults the wind for which $0 \leq p' \leq R_*$ and $z' < 0$, there will be rays which intercept the star that will have line frequencies *without* observable resonances. Taking this into account, and assuming that $\mathbf{v}(r = R_*) = 0$ on the stellar surface, the Sobolev line intensity is given by

$$I_\nu(p', \phi', z' \to \infty) \;=\; \begin{cases} I_\nu^{\rm core} \;\; , & 0 \leq p' \leq R_* \, , \; x < 0 \\ I_\nu^{\rm core} e^{-\tau_o^*} + \bar{S}(1 - e^{-\tau_o^*}) \;\; , & 0 \leq p' \leq R_* \, , \; x \geq 0 \\ \bar{S}(1 - e^{-\tau_o^*}) \;\; , & p' > R_* \;\; , \end{cases} \tag{3.19}$$

and τ_o^* is the Sobolev optical depth (eq. [2.35]) evaluated at the resonance point where $x = \hat{\mathbf{n}} \cdot \mathbf{v}/v_{th}$. Castor & Lamers (1979) take into account the underlying photospheric line absorption profile in $I_\nu^{\rm core}$, and find that it can significantly affect the wind profile shape where absorption is appreciable. The major effect is a weakening of the emission component of the overall line, and Castor & Lamers provide an approximate method of estimating this reduction:

$$\mathcal{R}_\nu \;\approx\; qE_\nu + \mathcal{R}_\nu^*(1 - A_\nu) \;\; , \tag{3.20}$$

where $\mathcal{R}_\nu^*$ is the photospheric line residual flux, $(1 - A_\nu)$ and E_ν are the direct ("absorption," from $I_\nu^{\rm core}$) and diffuse ("emission," from $\bar{S}$) components of the wind residual flux, and q is a fractional photospheric dimunition factor defined as

$$q \;\equiv\; \frac{v_{th}}{v_\infty} \int_{x=0}^{v_\infty / v_{th}} \mathcal{R}_\nu^*(x)\, dx \;\; , \tag{3.21}$$

which approaches unity in the limit of no photospheric absorption. Castor & Lamers (1979) find that this dimunition of the emission component of a P Cygni line is the

dominant effect of photospheric absorption, and find much better agreement between a self-consistent solution (with the absorption in $I_\nu^{\rm core}$) and eq. (3.20) than by using the simpler additive approximation of $\mathcal{R}_\nu \approx E_\nu + \mathcal{R}_\nu^* - A_\nu$.

The sign convention used above for the line velocity denotes $x > 0$ as velocities blueshifted toward the observer, and $x < 0$ as velocities redshifted away from the observer. This is opposite to the sign convention often used when dealing with observational data. The above form for the intensity (eq. [3.19]) reveals the existence of the blueshifted absorption trough in P Cygni lines, since blueshifted frequencies experience extra attenuation (in the $I_\nu^{\rm core} e^{-\tau_o^*}$ term) due to line resonances directly in front of the stellar disk. The emission from the diffuse wind-scattered radiation (in the $\bar{S}$ terms) is almost symmetric about line center because it is dominated by the large volume $p' > R_*$, but occultation effects give the red side slightly less emission.

Despite the qualitative success of using the Sobolev approximation to compute line profiles from hot-star winds (e.g., Castor & Lamers 1979), there exist significant quantitative differences between theoretical and observed P Cygni type line profiles. Most notably, strong saturated wind lines, e.g., the C IV $\lambda\lambda$1548, 1551Å doublet, have broad (hundreds of km s^{-1} wide) blueshifted "black troughs," while pure Sobolev theoretical profiles dip down to zero intensity only at one point: the terminal velocity. Lucy (1982, 1983) suggested that this broadening can be caused by multiple scattering between nonmonotonic velocity features in a wind, and this clearly indicates that Sobolev theory is inadequate to treat the radiative transfer in such lines. An alternative and very accurate method of generating wind profiles is to solve the equation of radiative transfer in the comoving frame (CF) of the wind (Mihalas, Kunasz, & Hummer 1975; Hamann 1981). Computationally, however, this method is significantly more expensive than the Sobolev approximation, and thus is impractical for use in interactive spectral analysis.

Lamers, Cerruti-Sola, & Perinotto (1987) have introduced an efficient technique for computing wind line profiles with an accuracy intermediate between the Sobolev approximation and the CF method. Their "Sobolev with Exact Integration" (SEI) algorithm uses the Sobolev escape probability form of the source function $\bar{S}$, but does not assume the simple "step function" solution to the equation of radiative transfer (i.e., it uses eq. [3.1] instead of eq. [3.3]). Hamann (1981) showed that most of the errors incurred in the pure Sobolev approximation come from this integration and not from the source function itself. Thus, the SEI intensity is given by

$$I_\nu(z' \to \infty) = \begin{cases} \int_{z_*}^{+\infty} \left[\kappa_L \, \rho \, \phi\left(x - \hat{\mathbf{n}} \cdot \mathbf{v}/v_{th}\right) \bar{S} \, e^{-\tau_\nu}\right] dz' \; + \; I_\nu^{\rm core} e^{-\tau_\nu} \;\; , & p' \le R_* \\ \int_{-\infty}^{+\infty} \left[\kappa_L \, \rho \, \phi\left(x - \hat{\mathbf{n}} \cdot \mathbf{v}/v_{th}\right) \bar{S} \, e^{-\tau_\nu}\right] dz' \;\; , & p' > R_* \end{cases} \tag{3.22}$$

where $z_* = (R_*^2 - p'^2)^{1/2}$ is the z' coordinate of the stellar surface. The optical depth must be integrated together with the intensity, and is given by

$$\tau_\nu(z') \;=\; \int_{z'}^{+\infty} \kappa_L \, \rho \, \phi \left(x - \frac{\hat{\mathbf{n}} \cdot \mathbf{v}}{v_{th}} \right) dz'' \;\; . \tag{3.23}$$

Note, however, that in the absence of the nonmonotonic velocities which generate black troughs, the Sobolev, SEI, and CF methods all give virtually identical results, and it is the need to model the complex observations which demands moving beyond pure Sobolev line profiles.

We utilize the SEI method in all models presented here, and we perform the "exact integration" for the line flux using the cylindrical (p', ϕ', z') coordinate system with the observer oriented along the positive z'-axis. The equation of radiative transfer is evaluated in differential form along rays parallel to this axis, and along each ray the optical depth and specific intensity are integrated using second order implicit Euler differencing. The resulting emergent intensities at the outer boundary of the computational grid are then integrated by nested Romberg quadrature in p' and ϕ' to form the flux, and this process is repeated for each frequency point in the total line profile.

3.1.3 Line Broadening and Opacity

The detailed atomic physics of the line transition to be modeled enters the problem in the profile function $\phi(x)$ and the line absorption coefficient κ_L. For simplicity, we assume a Doppler-broadened Gaussian line-profile function of the form

$$\phi(x) \;=\; \frac{\exp(-x^2)}{\sqrt{\pi}} \;\; , \tag{3.24}$$

but for lines with appreciable collisional damping, the normalized Voigt function

$$\phi(x, a) \;=\; \frac{a}{\pi^{3/2}} \int_{-\infty}^{+\infty} \frac{\exp(-y^2)\, dy}{a^2 + (x - y)^2} \tag{3.25}$$

can be used, where the Voigt parameter a is the ratio of the collisional to the Doppler broadening width,

$$a \;=\; \frac{c,}{4\pi\nu_o v_{th}} \;\; , \tag{3.26}$$

and , is the combined damping rate for natural (radiation) and collisional broadening (see Mihalas 1978).

The profile-integrated opacity or strength of a spectral line is given by

$$\chi_L(r) \;\equiv\; \kappa_L(r)\rho(r) \;=\; \frac{\pi e^2}{m_e c} \frac{1}{\Delta\nu_D} (gf)_{\ell u} \left(\frac{n_\ell}{g_\ell} - \frac{n_u}{g_u} \right) \;\; , \tag{3.27}$$

where u and ℓ denote the upper and lower levels of the atomic transition, f is the oscillator strength, and g is the multiplicity of the level. Because of the non-LTE conditions typical in extended atmospheres (and because most of the lines to be modeled are resonance lines), we can assume $n_\ell \gg n_u$ and write

$$(gf)_{\ell u}\left(\frac{n_\ell}{g_\ell} - \frac{n_u}{g_u}\right) \approx f_{\ell u}\, n_\ell = f_{\ell u}\, q_i\, A\, X \frac{\rho}{m_H} \quad , \tag{3.28}$$

where q_i is the fraction of the element in the ith ionization state and A is its elemental abundance (by number) relative to hydrogen. The primary radial variation in χ_L, then, comes from the ionization fraction q_i and the density ρ, and we can write the line absorption coefficient as

$$\kappa_L(r) = \left[\frac{\pi e^2}{m_e c}\,\frac{f_{\ell u} A X}{m_H \Delta\nu_D}\right] q_i(r) \equiv \kappa_0 \left[\frac{q_i(r)}{q_0}\right] \quad , \tag{3.29}$$

where q_0 is the ionization fraction at a specified radius (typically taken where $v_r \approx v_\infty/2$).

Following the notation of POF, let us parameterize the constant coefficient κ_0 by defining a dimensionless line strength

$$k_L \equiv \left(\frac{\dot{M} v_{th}}{4\pi R_* v_\infty^2}\right)\kappa_0 \quad , \tag{3.30}$$

where v_∞ and $\dot{M}$ are taken from a simple one-dimensional steady-state wind model. POF assume $\kappa_L = \kappa_0$, which is valid for some lines of interest in the dominant ionization stage of the wind. However, Bjorkman et al. (1994) discuss various relevant parameterizations for the ionization fraction $q_i(r)$, and use a combined scaling law of the form

$$q_i(r) \propto \left(\frac{\rho}{W}\right)^{-\Delta i}\left(\frac{R_*}{r}\right)^{\gamma} \quad , \tag{3.31}$$

where the first term represents the ionization fraction in a case where the ionization rates are dominated by photoionization and radiative recombination (see Section 2.2.5), and Δi is the difference between the ion stage i and the dominant stage. The second term above results from an empirical opacity fit used by Lamers et al. (1987) and others to model weak lines which lack sharp "edges" in the blueshifted P Cygni absorption troughs.

In order to produce line profiles that best resemble the observations, one additional assumption is often included in the theoretical description of the line profile strength and shape: the presence of "turbulent" velocities. On the smallest scales,

microturbulent velocities can be convolved with the thermal Maxwellian motions of the gas, and an effective Doppler width of the form

$$\Delta\nu_D \;=\; \frac{\nu_o}{c}\sqrt{v_{th}^2 + v_{\rm turb}^2} \tag{3.32}$$

can be assumed. Although most implementations assume a constant microturbulent velocity of the order 50–200 km s^{-1}, better line profile fits have been obtained by assuming that $v_{\rm turb}$ varies in proportion to the mean wind velocity $v_r(r)$ (Haser et al. 1995). Also, for a large sample of B stars, Denissenkov (1994) found that the photospheric microturbulent velocity correlates well with the projected rotation velocity $V_{\rm eq}\sin i$, and this may be useful for empirical models of wind lines from rapidly rotating Be stars.

POF found that a better physical explanation for the effects of "microturbulent broadening" is the presence of stochastic small-scale instability shocks in line-driven winds. Following Lucy's (1982, 1983) conjecture that multiply nonmonotonic shocked velocity laws can explain the broadened black troughs in saturated P Cygni resonance lines, POF computed the nonlocal multiple-resonance source function for a highly structured unstable wind model, and indeed found similar broadening to that produced by ad-hoc microturbulence. However, note that multiple scattering and microturbulence produce black troughs for different reasons. When a non-monotonic velocity structure is present, the increased back-scattering from multiple resonances creates *reduced emission* on the blue side of the line. When microturbulent broadening is present, though, it produces a greater velocity dispersion in the single uncoupled resonance zones, *separating* the redshifted emission from the blueshifted absorption and resulting in a widened line trough. Despite these differences the computed line profiles are morphologically similar, and we apply the simpler microturbulence picture in the line profiles computed in this dissertation.

3.1.4 Examples of SEI P Cygni Line Profiles

We have developed a fully multidimensional code which implements the Sobolev and SEI methods of constructing P Cygni line profiles from expanding winds. Here we present examples of such idealized spectral lines using the one-dimensional ζ Puppis wind model discussed above in Chapter 2. The radial velocity and density, as computed numerically by VH-1, are read into the SEI code, and spherical symmetry is assumed in this case. The "standard" line profile parameters we choose are: $k_L = 1$ (a moderate unsaturated line), $\epsilon_o = 0$ (a pure-scattering resonance line), $v_{\rm turb} = 100\,{\rm km\ s^{-1}}$ (as is required observationally to approximate small-scale instability structure), and $\Delta i = \gamma = 0$ (for a line in the dominant ionization stage of the wind; e.g., as in POF).

Figures 3.1–3.4 show the computed SEI line profiles, plotted versus Doppler line velocity in the star's frame, for variations of the above standard parameters. Figure 3.1 varies the line strength k_L by two orders of magnitude above and below the standard value of unity, while keeping the other parameters fixed. Note that for $k_L \gtrsim 10$ the line is fully saturated, and any extra opacity has a negligible impact on the profile shape. Also, the deepest blueshifted absorption for *weak* lines occurs several hundred km s^{-1} below the maximum model velocity (here, $\sim$2800 km s^{-1}), which implies that observational estimates of v_∞ may be slightly underestimated if *unsaturated* P Cygni absorption troughs are used to determine them. Figure 3.2 shows the standard $k_L = 1$ line, but varies the artificial microturbulent velocity. The sharp profile corresponding to $v_{\rm turb} = 0$ km s^{-1} is virtually identical to the line profile generated by the pure Sobolev method discussed above (see also Lamers et al. 1987). Figure 3.3 also varies $v_{\rm turb}$, but for a strong *saturated* P Cygni line with $k_L = 100$; note the black troughs generated by the increased velocity dispersion.

Following the initial models of Castor (1970), which implied that strong Wolf-Rayet emission lines may be merely the result of thermal emission in an expanding wind, we have varied the collisional probability $\bar{\epsilon}$ according to eq. (3.9). Figure 3.4 shows the result of varying the constant ϵ_o, and allowing the true ratio of collisional to radiative deexcitations ($\bar{\epsilon}'$) to remain proportional to the wind density. We choose the normalizing constant ρ_o in eq. (3.9) to be the maximum (base) density of the model, which implies that rather large values of ϵ_o (close to unity) are required to produce significant emission in the majority of the accelerating wind. Note, however, that many strong Wolf-Rayet lines are recombination, not resonant, transitions, and the line absorption coefficient κ_L depends on the density of the wind because of the need to populate the lower level. The actual line profiles are thus roughly similar to those using an ionization law of the form eq. (3.31), with $\gamma \approx 2$. The profile shapes, then, are "damped out" at high velocities, and often do not show blueshifted P Cygni absorption (see, e.g., Bjorkman et al. 1994).

3.2 Continuum Polarization

Well before Maxwell's theoretical exposition of classical electromagnetism in 1864, the nature of light propagating via transverse waves was generally accepted from empirical evidence. Stokes (1852) showed that any collection of such waves can be characterized by four independent parameters which describe its intensity, geometry, and phase distribution; i.e., the *polarization* state of the wave. If the intensity I of a light beam is measured with respect to a given set of axes, its projected components in two perpendicular planes (their normals also perpendicular to the direction of propagation) can be denoted I_ℓ and I_r. The addition of two or more electric field vectors of the radiation components will, in the most general case,

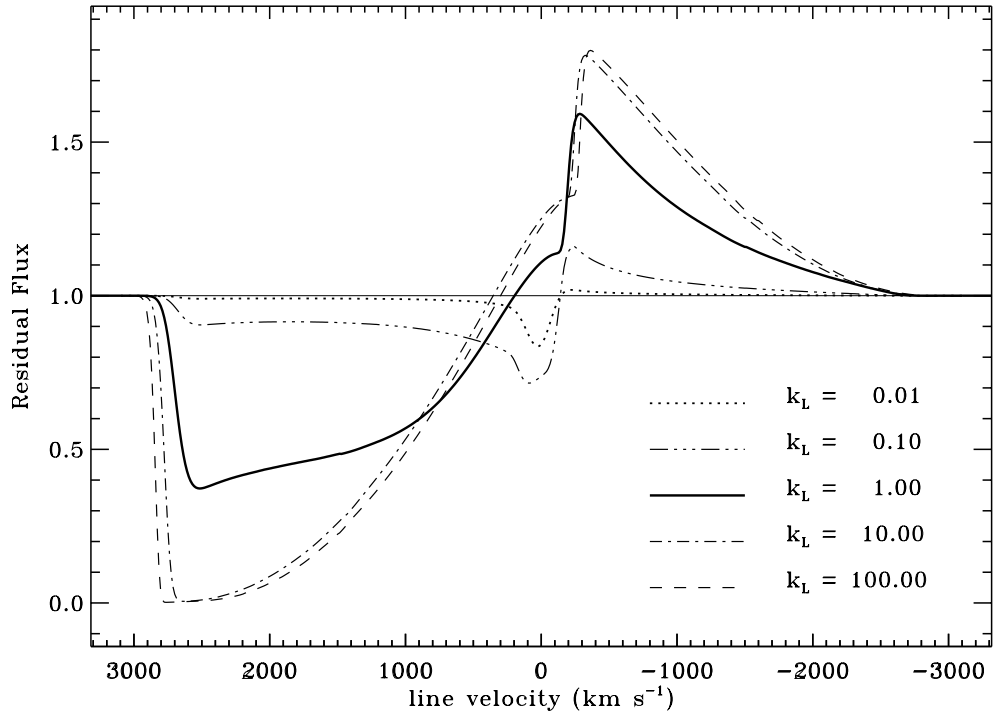

Figure 3.1: P Cygni line profiles, generated by the SEI method, for the standard ζ Puppis model wind. This figure varies the line strength by two orders of magnitude above and below the standard, moderately unsaturated value.

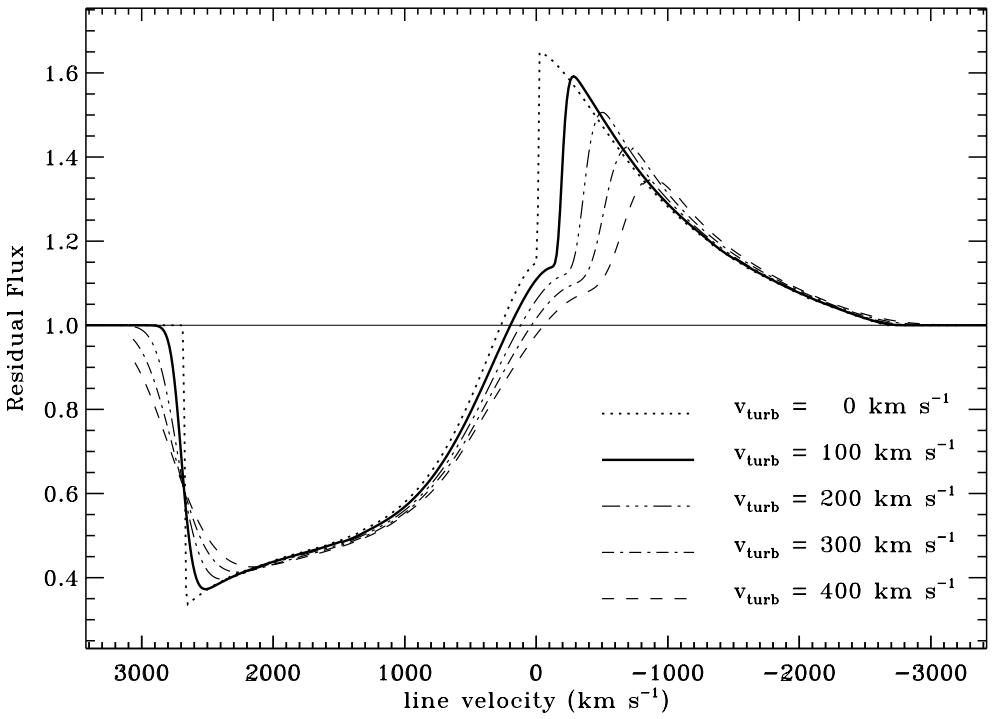

Figure 3.2: P Cygni line profiles, generated by the SEI method, for the standard ζ Puppis model wind. This figure varies the artificial microturbulent velocity above and below the standard value.

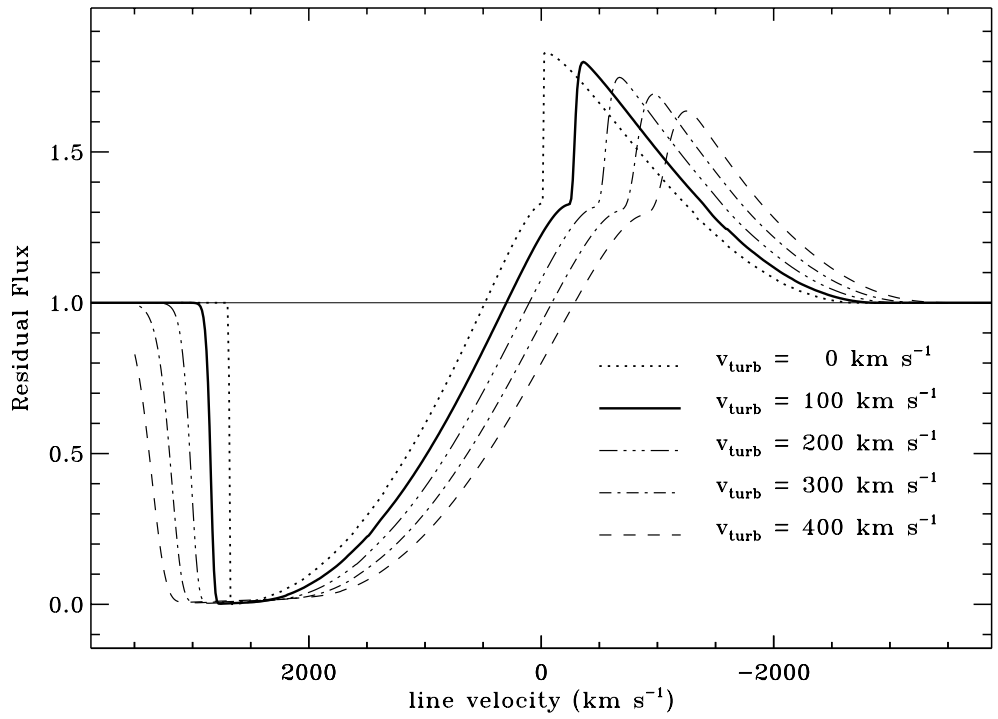

Figure 3.3: P Cygni line profiles, generated by the SEI method, for a strong *saturated* line with 100 times the line strength of the standard model, but using all other standard ζ Puppis parameters. This figure varies the artificial microturbulent velocity above and below the standard value.

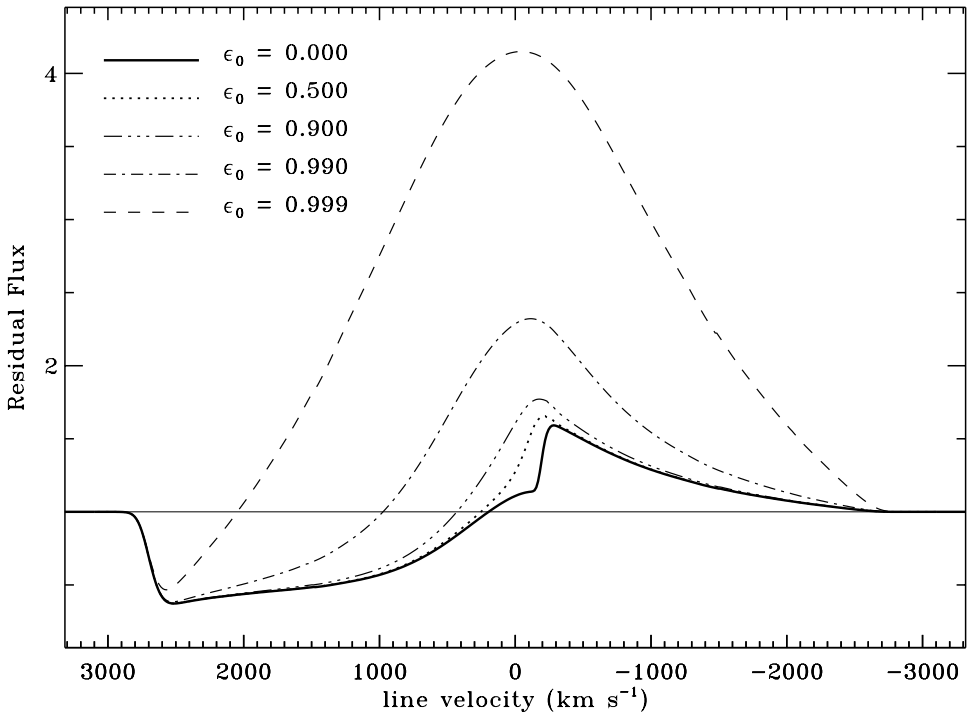

Figure 3.4: P Cygni line profiles, generated by the SEI method, for the standard ζ Puppis model wind. This figure varies the scaled probability of collisional deexcitations, from zero (pure scattering) to values approaching unity (pure thermal emission).

result in a vector whose tip traces out an elliptically helical spiral as it propagates through space. If this ellipse is oriented with an angle θ to the ℓ-reference axis and has an ellipticity (ratio of semiminor to semimajor axes) of $\tan\phi$, the four intensity-like Stokes parameters can be defined as

$$I = (I_\ell + I_r) \tag{3.33}$$
$$Q = (I_\ell - I_r) \tag{3.34}$$
$$U = (I_\ell - I_r)\,\tan 2\theta \tag{3.35}$$
$$V = (I_\ell - I_r)\,\sec 2\theta\,\tan 2\phi \tag{3.36}$$

(see, e.g., Collins 1989). This represents a single *elliptically polarized* and monochromatic beam, expressible most generally as a function of only three independent variables (I, θ, ϕ) since I_ℓ and I_r can be written in terms of each other via

$$\frac{I_\ell}{I_r} = \frac{1 + \cos 2\theta \cos 2\phi}{1 - \cos 2\theta \cos 2\phi} \ . \tag{3.37}$$

For $\phi = \pm\pi/4$ (or $Q = U = 0$) the beam traces out a circular path, and is considered *circularly polarized.* For $\phi = 0$ or $\pm\pi/2$ (or $V = 0$) the beam traces out a one-dimensional, but inclined path, and is considered *linearly polarized.* For all values of θ and ϕ, this "complete" polarization of a monochromatic beam results in $I^2 = Q^2 + U^2 + V^2$.

However, when observing an extended source such as a star, we observe an unresolved collection of many electromagnetic waves, each with its own polarization, convolved together into a single time-averaged intensity. By passing this radiation through, e.g., polarizing filters and quarter-wave plates, we can obtain some information about its overall polarization state. Redefining the above Stokes parameters as the appropriate averages over the incident beams (see Rybicki & Lightman 1979), we obtain the inequality

$$I^2 \geq Q^2 + U^2 + V^2 \ , \tag{3.38}$$

and in the extreme limit of a totally random distribution, $Q = U = V = 0$, and the beam is considered *unpolarized.* Anticipating observations of polarization from stars, let us define the degree of linear polarization P and the position angle Ψ,

$$P \equiv \frac{\sqrt{Q^2 + U^2}}{I} \ , \qquad \tan 2\Psi \equiv \frac{U}{Q} \ , \tag{3.39}$$

and for a completely polarized beam, the position angle Ψ and the ellipse angle θ are equivalent.

Note that the Stokes parameters I and V are invariant under coordinate rotations about the axis of propagation, but Q and U are not. Thus, when computing

the emergent Stokes intensities from a heterogeneous and extended collection of emitters, it becomes necessary to refer the four components due to each emitter to the same set of axes. This is achieved by rotating the vector-like intensity through an angle ψ,

$$\begin{pmatrix} I' \\ Q' \\ U' \\ V' \end{pmatrix} = \begin{pmatrix} 1 & 0 & 0 & 0 \\ 0 & \cos 2\psi & \sin 2\psi & 0 \\ 0 & -\sin 2\psi & \cos 2\psi & 0 \\ 0 & 0 & 0 & 1 \end{pmatrix} \begin{pmatrix} I \\ Q \\ U \\ V \end{pmatrix} , \tag{3.40}$$

where ψ is defined in practice as the angle between the chosen Q-axis for the entire region and the individual normal vectors to the scattering planes which produce the bulk of the polarized radiation.

The observation of polarization from stars is a difficult task. Although Chandrasekhar (1946) predicted that Thomson scattering in stellar atmospheres can give rise to as much as 12% local linear polarization at the limb, this effect averages to zero over a spherical star, for which there is no preferred plane on the sky. It was not until Kemp et al. (1983) observed a phase-dependent variation of polarization from the eclipsing binary Algol that this effect was actually confirmed from individual *portions* of an occulted star. A rapidly rotating star will also exhibit a small degree of atmospheric polarization ($\sim$0.1%) because oblateness and gravity darkening create a preferred plane on the sky (Rucinski 1970; Collins, Truax, & Cranmer 1991). In addition, Collins & Cranmer (1991) predicted that rapidly rotating stars, which produce Doppler-broadened absorption line profiles, should exhibit a slightly stronger variation in linear polarization across these "spatially filtered" lines.

In this work, however, we are mainly concerned with the polarization due to the circumstellar gas, and we will assume the incident light from the star is initially unpolarized. Many classes of hot stars which exhibit emission lines (Be, Of, Wolf-Rayet stars) are also observed to have significant ($\sim$ 1–2%) linear polarization, and this is assumed to come from an asymmetric outer envelope (see, e.g., Zellner & Serkowski 1972; Coyne & McLean 1982; Schmidt 1988). The polarization of Be stars is commonly interpreted as arising from Thomson scattering of photospheric radiation in a rotationally-flattened envelope or disk. Because the circumstellar environments of most O and B stars are *optically thin* to continuum radiation, let us follow Brown et al. (1978) and Wood et al. (1993) in treating this region as a single-scattering medium, thus ignoring absorption, local emission, and multiple-scattering of photons (see, however, Wood et al. 1996). The formal solution to the equation of radiative transfer (eq. [3.1]), in the limit of the scattered radiation dominating the

direct stellar radiation, reduces in the optically thin limit to

$$I_\nu \approx \int_0^{\tau_\nu} S_\nu(t_\nu)\, dt_\nu \approx \int_{-\infty}^{+\infty} \sigma_e\, \rho\, S_\nu\, dz' \quad . \tag{3.41}$$

Representing all intensity-like quantities as four-component Stokes vectors, the flux can be written as

$$\boldsymbol{\mathcal{F}}_\nu = \begin{pmatrix} \mathcal{F}_\nu^I \\ \mathcal{F}_\nu^Q \\ \mathcal{F}_\nu^U \\ \mathcal{F}_\nu^V \end{pmatrix} = \frac{1}{r^2} \int_{\phi'=0}^{2\pi} \int_{p'=0}^{+\infty} \begin{pmatrix} I_\nu^I \\ I_\nu^Q \\ I_\nu^U \\ I_\nu^V \end{pmatrix} p'\, dp'\, d\phi' \quad , \tag{3.42}$$

which is effectively a volume integral over the optically thin scattering envelope,

$$\boldsymbol{\mathcal{F}}_\nu = \frac{1}{D^2} \int_{V_*} \sigma_e\, \rho\, \mathbf{S}_\nu\, dV_* \quad , \tag{3.43}$$

where the distance from the observer to the envelope D is considered much larger than the internal dimensions of the envelope.

The four-component Stokes source function for the Thomson scattering must be evaluated to take into account the geometrical effects of scattering between the ℓ and r polarization planes. Assuming coherent scattering, the source function can be written as

$$\mathbf{S}_\nu(\Omega) = \frac{1}{4\pi} \oint \mathbf{R}(\Omega, \Omega')\, \mathbf{I}_\nu^*(\Omega')\, d\Omega' \quad , \tag{3.44}$$

where the incident intensity is assumed to be unpolarized,

$$\mathbf{I}_\nu^* = \begin{pmatrix} I_\nu^{\text{core}} \\ 0 \\ 0 \\ 0 \end{pmatrix} \tag{3.45}$$

and the 4×4 redistribution matrix $\mathbf{R}$ is the *product* between a Rayleigh phase matrix which takes into account local scattering between the four Stokes components, and the rotation matrix given above (eq. [3.40]) which affixes each scattering into a

single coordinate frame. When this matrix is multiplied by the unpolarized incident intensity vector (see Wood et al. 1993 for details), the source function becomes

$$\mathbf{S}_\nu \;=\; \begin{pmatrix} S_\nu^I \\ S_\nu^Q \\ S_\nu^U \\ S_\nu^V \end{pmatrix} \;=\; \frac{3}{16\pi} \oint I_\nu^{\rm core} \begin{pmatrix} 1+\cos^2\chi \\ \sin^2\chi\,\cos 2\psi \\ -\sin^2\chi\,\sin 2\psi \\ 0 \end{pmatrix} d\Omega' \quad , \tag{3.46}$$

where $\chi = \cos^{-1}(\hat{\mathbf{n}}\cdot\hat{\mathbf{n}}')$ is the scattering angle between the direction of incident radiation $\hat{\mathbf{n}}'$ and the direction pointing to the observer $\hat{\mathbf{n}}$. Note that all V-components are thus zero, implying *linear* polarization of circumstellar envelopes. (Stars with magnetic fields, however, will have a non-zero V polarization due to the Zeeman effect; see Collins 1988.)

For the simple cases of a point source and a spherical, uniformly-bright star at the origin, the angles χ and ψ are evaluated in a straightforward manner, and eq. (3.43) above can be integrated over the source volume V_* and incident solid angles Ω' to determine the emergent Stokes fluxes. The normalized degree of linear polarization and position angle are defined by Wood et al. (1993) as

$$P_\nu \;\equiv\; \frac{\sqrt{(\mathcal{F}_\nu^Q)^2+(\mathcal{F}_\nu^U)^2}}{\mathcal{F}_\nu^I+\mathcal{F}_\nu^{\rm core}} \quad , \qquad \Psi_\nu \;\equiv\; \frac{1}{2}\tan^{-1}\left(\frac{\mathcal{F}_\nu^U}{\mathcal{F}_\nu^Q}\right) \quad , \tag{3.47}$$

where the direct "core" flux is given for a spherical star at the origin by

$$\mathcal{F}_\nu^{\rm core} \;=\; \oint I_\nu^{\rm core}\,\mu'\,d\mu'\,d\phi' \;\approx\; \frac{\pi R_*^2}{D^2}\,I_\nu^{\rm core} \quad . \tag{3.48}$$

Brown et al. (1978), Bjorkman (1992), and Wood et al. (1993) performed the above volume and solid angle integrals for various geometries and derived several useful analytic formulae for P_ν and Ψ_ν for the case of an axisymmetric disk-like density enhancement. Specifically, if one ignores the occultation of material behind the star, one obtains the particularly simple result for such a disk:

$$\mathcal{F}_\nu^Q \;\propto\; \sin^2 i \quad , \qquad \mathcal{F}_\nu^U \;=\; 0 \quad , \tag{3.49}$$

and this potentially allows the separation of such inclination-dependent quantities as $V_{\rm eq}\sin i$. Brown (1994) reviewed various applications of the above theory to observations of Be star disks, axisymmetric and expanding winds, and even time-dependent inhomogeneities in winds such as the small-scale "blobs" inferred from Wolf-Rayet emission lines. In subsequent Chapters we will numerically compute the polarization from winds with large-scale rotational structure, with the eventual goal of comparing these theoretical values with observations.